Active CMOS Sensor Array for Electrochemical Biomolecular Detection

Peter M. Levine, *Student Member, IEEE*, Ping Gong, Rastislav Levicky, and Kenneth L. Shepard, *Fellow, IEEE*

***Abstract*—Electrochemical sensing of biomolecules eliminates the need for the bulky and expensive optical instrumentation required in traditional fluorescence-based sensing assays. Integration of the sensor interface electrodes and active electrochemical detection circuitry on a CMOS substrate miniaturizes the sensing platform, enhancing its portability for use in point-of-care applications, while enabling the high-throughput, highly parallel analysis characteristic of traditional microarrays. This paper describes the design of a four-by-four active sensor array for multiplexed electrochemical biomolecular detection in a standard 0.25-μm CMOS process. Integrated potentiostats, comprised of control amplifiers and dual-slope analog-to-digital converters, stimulate the electrochemical cell and detect the current flowing through the on-chip gold electrodes at each sensor site that results from biomolecular reactions occurring on the chip surface. Post-processing steps needed to fabricate a biologically-compatible surface-electrode array in CMOS that can withstand operation in a harsh electrochemical environment are also described. Experimental results demonstrating the proper operation of the active CMOS array for biomolecular detection include cyclic voltammetry of a reversible redox species, DNA probe density characterization, as well as quantitative and specific DNA hybridization detection.**

***Index Terms*—Biosensor, cyclic voltammetry, DNA, electrochemical sensor, microelectrode, potentiostat.**

I. Introduction

QUANTITATIVE and specific detection of biomolecules such as DNA and proteins has numerous applications in biomedical diagnostics and environmental monitoring. DNA sensing, in particular, has broad application in genotyping, gene-expression studies, mutation detection, pharmacogenomics, forensics, and related fields in which genetic content provides crucial insight into biological function or identity [1], [2].

Manuscript received December 14, 2007; revised March 12, 2008. Published July 23, 2008 (projected). This work was supported in part by the National Human Genome Research Institute under Grant R33HG003089. The content is solely the responsibility of the authors and does not necessarily represent the official views of the National Human Genome Research Institute or the National Institutes of Health. This work was also supported in part by the Semiconductor Research Corporation (SRC) Center for Circuit and System Solutions (C2S2), the Catalyst Foundation, and an Intel Foundation Ph.D. Fellowship.

P. M. Levine and K. L. Shepard are with the Department of Electrical Engineering, Columbia University, New York, NY 10027 USA (e-mail: plevine@cisl.columbia.edu; shepard@ee.columbia.edu).

P. Gong is with the Departments of Chemical Engineering and Electrical Engineering, Columbia University, New York, NY 10027 USA (e-mail: gongping@cisl.columbia.edu).

R. Levicky is with the Department of Chemical and Biological Engineering, Polytechnic University, Brooklyn, NY 11201 USA (e-mail: rlevicky@poly.edu).

Digital Object Identifier 10.1109/JSSC.2008.925407

High-throughput, multiplexed DNA analysis is usually performed in a laboratory environment using a "microarray", a passive substrate (such as a glass slide) on which thousands of single-stranded DNA (ssDNA) "probe" molecules arranged in a regular pattern bind to (or "hybridize" with) fluorophore-labeled "target" molecules in an unknown analyte solution. Probes can be synthesized externally and then immobilized on the microarray through mechanical contact spotting or non-contact ink-jet printing [1], or can be constructed *in situ* using photolithographic techniques and solid-phase chemical synthesis [3]. Hybridization occurs when the probe and target sequences are complementary to each other. Microarray scanners, employing laser sources and photomultiplier tubes or charge-coupled device (CCD) cameras that excite the fluorophores and detect the emitted light, can measure surface-bound target densities down to 10^6 cm^{-2} [4]. However, fluorescent techniques, in addition to requiring labeled targets, require bulky and expensive instrumentation, defying portability for point-of-care applications.

Electrochemical sensing approaches to DNA detection, which have gained interest in recent years but are not yet as well-developed as optical techniques [5], rely on detecting changes occurring with hybridization at the interface between a metal "working" electrode (WE), functionalized with probe molecules, and a conductive target analyte solution. Electrochemical measurement techniques have the potential to provide real-time, label-free sensing and more portable detection platforms [6]. A feedback circuit known as a "potentiostat" is used to apply a desired potential across the WE interface and measure the resulting current. If the target molecules are conjugated with "redox" labels [chemical species which gain electrons (undergo reduction) or lose electrons (undergo oxidation) due to an applied potential], probe-target binding can be detected by measuring changes in the direct (Faradaic) current flowing across the interface [7]. Alternatively, it may be possible to perform label-free sensing by measuring only changes in displacement (non-Faradaic) current at the interface that occur due to surface-charge fluctuations [8]. Label-free sensing approaches eliminate numerous steps in target analyte preparation, reducing time and cost.

Microarray applications based on electrochemical sensing ultimately demand parallel detection of hundreds to thousands of sensing sites. This requires active multiplexing that can only be achieved through integration of the WEs directly onto an active CMOS substrate containing the sensor electronics. Previous work in CMOS electrochemical sensors include a sensor chip interfaced to a single off-chip WE as shown in Fig. 1(a), where all chemical reactions are carried out off chip [9], [10], and arrays of on-chip electronic sensing elements interfaced to individual off-chip WEs [11], as displayed in Fig. 1(b). Although

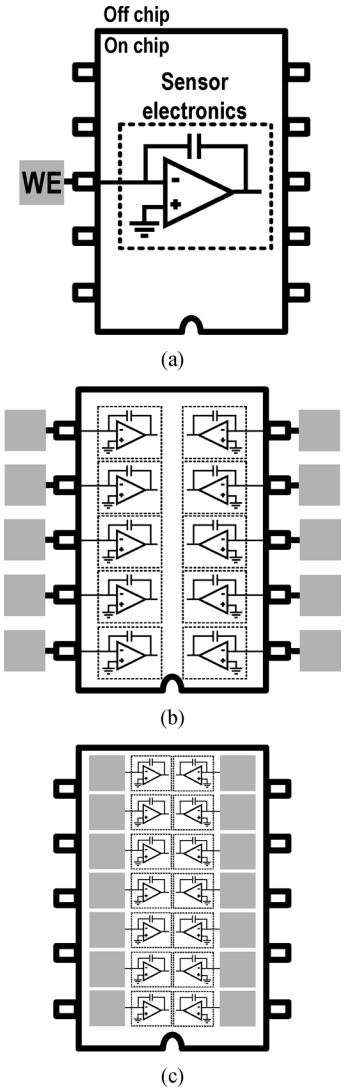

Fig. 1. CMOS electrochemical-sensor implementations. (a) Sensor chip interfaced with one off-chip working electrode (WE). (b) Array of on-chip sensing elements connected individually to off-chip WEs. (c) Integration of arrays of sensing elements with on-chip WEs, where all electrochemical reactions are carried out directly on the chip surface.

CMOS sensors consisting of a single on-chip WE and potentiostat have been constructed [12], much of the most recent work on integrated electrochemical sensors focuses on the integration of entire WE arrays on the same CMOS substrate as the sensor electronics [13]–[18], as shown in Fig. 1(c).

Prior work in CMOS-based electrochemical sensing arrays for biomolecular detection has focused on specific modalities of potentiostatic sensing, such as redox cycling [13] and capacitance-to-frequency conversion [15], to simplify the electronics. However, due to the complexity of electrochemical biomolecular analysis, we believe that general potentiostatic functionality is best suited to this application. Therefore, in this work, we design an array of such generalized high-performance potentiostats with integrated WEs [19]. In addition, because we are developing one of the first generalized substrates for electrochemical DNA sensing, protocols for electrochemical detection are created along with the sensing chip. These enable our active CMOS array to perform quantitative electrochemical DNA detection in a manner consistent with fluorescence-based microarrays.

This paper is organized as follows. Section II provides background on potentiostat operation and electrochemical sensing. Section III describes the design of the active CMOS sensor array and discusses chip processing and packaging issues. Section IV includes experimental results from electrical characterization of the array as well as electrochemical results using the active CMOS sensor array to measure redox species, determine DNA probe coverages, and perform sensing of DNA probe-target hybridization on chip. In addition, analysis of the effect of various noise sources on the sensor detection limit is included in this section. The paper is concluded in Section V.

II. Electrochemical Sensing

This section describes potentiostat operation in detail and discusses "cyclic voltammetry", a classical electrochemical measurement technique, as it applies to our electrochemical sensor array.

A. Potentiostat Operation

A potentiostat is a feedback control system used to apply a desired potential to an electrochemical cell and to measure simultaneously the movement of charge through the cell that accompanies electrochemical reactions occurring at an electrode–electrolyte interface. A standard potentiostat used in a typical electrochemical setup, shown conceptually in Fig. 2(a), consists of three electrodes immersed in an electrolyte: a WE at which the reaction of interest occurs and to which biomolecular probes can be attached, a "reference" electrode (RE) to hold the electrolyte at a known potential, and a "counter" electrode (CE). The voltage V between WE and CE is adjusted to establish a desired cell input voltage V_{in} between the WE and RE. Direct current I can flow through the external circuit (as measured by the ammeter A) as redox species in the electrolyte, for example, donate electrons to the WE and accept electrons from the CE (through a Faradaic process). In addition, a displacement current can flow as ions segregate to the WE and CE to form space-charge regions (through a non-Faradaic process). The high-impedance voltmeter (VM) attached to the RE ensures that very low current flows through this interface, helping to maintain it at equilibrium.

The basic potentiostat circuitry in Fig. 2(a) can be implemented using standard electronic components as shown in Fig. 2(b). The operational amplifier (opamp) on the right establishes the control loop while the integrator on the left converts the current flowing through the WE to a voltage for digitization and readout. The high input impedance of the control amplifier ensures that only a very small current flows through the RE. This circuit can be implemented in a CMOS process and forms the basis of the integrated sensor array.

B. Cyclic Voltammetry

Different sensing modalities are determined by the nature of the input voltage applied to the potentiostat. We use cyclic voltammetry (CV), a low-speed, large-signal technique, to detect redox species, determine surface DNA probe concentration,

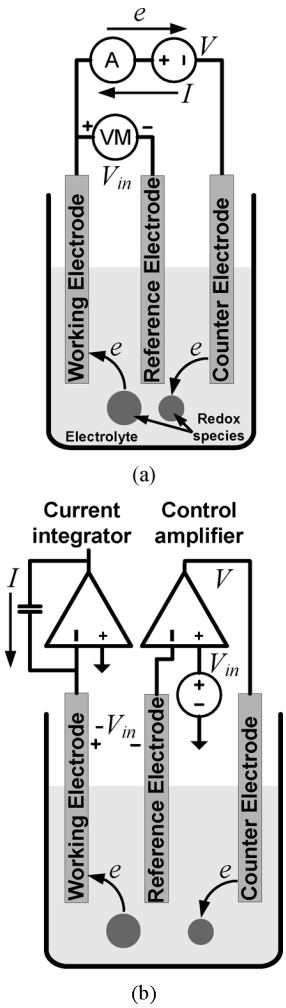

Fig. 2. Description of potentiostat operation. (a) Conceptual diagram. (b) Implementation using electronic components.

and measure DNA probe-target hybridization. In CV, V_{in} (always expressed relative to a standard RE potential, denoted here as V_{RE}) is set to the initial voltage V_i, ramped up to the vertex potential V_v at the scan rate ν, and then ramped down at the same rate until the final voltage V_f (usually equal to V_i) is reached, as shown in Fig. 3, while the current flowing through the WE I_{WE} is measured simultaneously. When detecting redox species present in solution, I_{WE} as a function of time appears as shown in Fig. 3. However, I_{WE} is normally viewed as a function of V_{in} so that the potentials at which reduction and oxidation occur (indicated by the forward and reverse current peaks, respectively) may be easily discerned. These potentials, as well as the value of I_{WE} at each peak, indicate the degree of reversibility of the electrochemical reaction as well as the amount of chemical product generated or reactant consumed [20].

III. Active CMOS Sensor Array Design

The architecture of the active CMOS sensor array is displayed in Fig. 4 and the die photograph is shown in Fig. 5. The chip has been fabricated in a TSMC 2.5-V, five-metal, 0.25-μm CMOS process and measures 5 mm by 3 mm. Each array site consists of a square gold (Au) WE and a dual-slope analog-to-digital converter (ADC) with digital control circuitry to digitize the

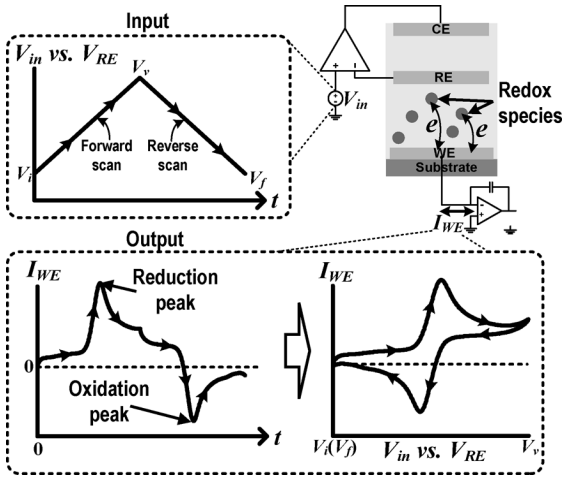

Fig. 3. Measurement of an electrochemical cell containing a redox species in solution using CV.

current flowing through the electrode. The WEs in the top row have a side length of 100 μm with WEs in the subsequent rows having lengths of 90, 80, and 70 μm. This variation allows us to study the effect of electrode area on the cell current for different redox and biomolecular reactions. Each row of four WEs shares a 15 μm by 2500 μm CE driven by a control amplifier. The components of the active CMOS sensor array, as well as post-processing and packaging issues, are described below.

A. Electrochemical Cell Model

To simulate system behavior and test potentiostat stability when the chip is operated in an electrolyte, the small-signal circuit model of the electrode–electrolyte interfaces in an electrochemical cell, shown in Fig. 6(a), is used [20]. In this model, resistors R_{s1} and R_{s2} represent the solution resistance between the WE and RE, and CE and RE, respectively. Based on impedance measurements of the electrochemical cell using a CHI 700C-series commercial potentiostat (CH Instruments, Austin, TX) with a 125-μm-diameter Au WE (ESA Biosciences, Chelmsford, MA), platinum-wire (Pt-wire) CE (Sigma-Aldrich), and a standard silver/silver-chloride/3-M sodium-chloride (Ag/AgCl/3-M NaCl) RE (Bioanalytical Systems, West Lafayette, IN), R_{s1} ranges from approximately 275 Ω in 1-M potassium phosphate buffer (PPB, pH 7.4) to 10 kΩ in 10 mM PPB. Capacitors C_{WE} and C_{CE} model the interfacial "double-layer" capacitance at the WE–electrolyte and CE–electrolyte interfaces, respectively. The measured value of C_{WE} is on the order of 1 to 100 μF cm^{-2}, depending on the electrolyte composition and modification of the WE surface. Resistors R_{ct1} and R_{ct2} model the charge-transfer resistance at each interface, with the former having a typical measured value between 1 MΩ and 10 MΩ. The use of a three-electrode potentiostat configuration makes the measurement of the WE interface independent of the RE and CE impedances. However, knowledge of the R_{s2}, R_{ct2}, and C_{CE} values is necessary to test amplifier stability when designing the active sensor array.

B. Potentiostat Circuits

The potentiostat circuits are designed to provide good noise performance and stability across a wide range of operating

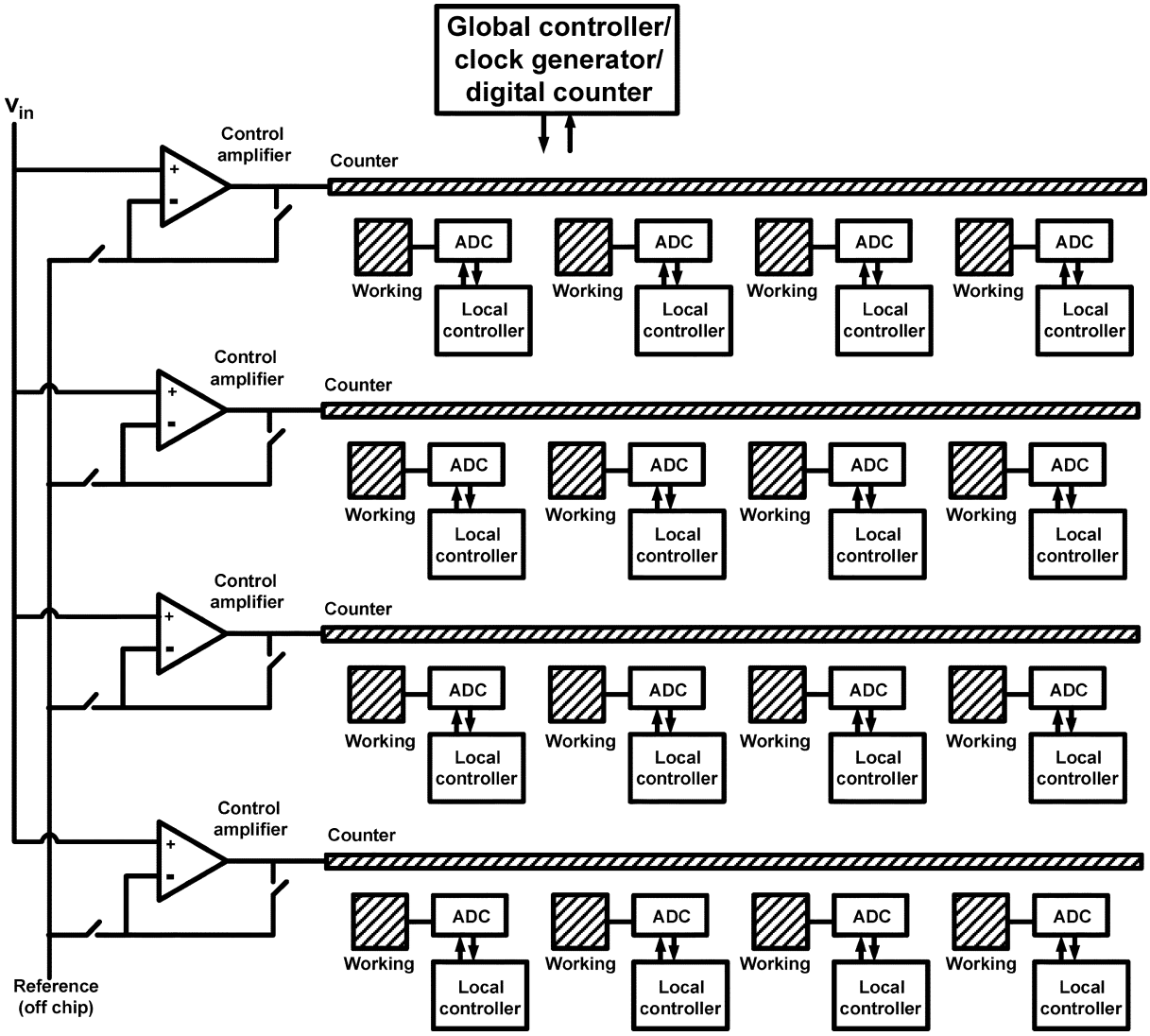

Fig. 4. Active CMOS sensor array architecture.

conditions. The control amplifier is implemented with a two-stage, single-ended-output opamp having a simulated DC gain of 87 dB. Since CV is usually carried out using low-frequency input signals, the amplifier contains input pMOS devices having a width and length of 4 mm and 1 μm, respectively, to reduce the effect of flicker $(1/f)$ noise on the output.

Based on electrochemical measurements of redox species and DNA probe-target hybridization experiments using a commercial potentiostat and a 125-μm-diameter WE, it is determined that the integrated ADCs must be able to digitize currents in the 100 pA to 250 nA range that flow bidirectionally through the WE. In addition, since the maximum effective frequency of the input voltage stimulus used in our CV experiments is about 100 Hz, ADC operation at sampling rates up to 10 kHz is sufficient to accurately reconstruct the cell current. A dual-slope ADC architecture [21], shown in Fig. 7(a), is selected for this purpose because its dynamic range, sampling frequency, and nominal resolution can all be easily adjusted. The ADC consists of an integrating amplifier with a fixed on-chip 5 pF linear capacitor, track-and-latch comparator, nMOS switches accompanied by "dummy" transistors to absorb injected charge during switching, and a digital counter with control logic. Fig. 7(b) displays the control signals, clocks, and integrator and comparator outputs for a typical ADC conversion cycle. After the integrator is reset during the period t_{rst}, current I_{WE} is integrated onto capacitor C_f for a fixed time interval t_1. During this period, the comparator clock ϕ_{clk}, which operates at a higher rate than the ADC sampling frequency f_s, is gated in order to reduce the effect of switching interference on the integrator output. After t_1, ϕ_{clk} is enabled and the integrator output voltage V_{int} is measured by the comparator during the period t_d. Based on the comparator output V_{comp}, the capacitor is discharged using the appropriate constant current source I_{ref+} or I_{ref-} (implemented using a pMOS and nMOS current mirror, respectively, biased with off-chip resistors) until V_{int} crosses the comparator threshold (set to analog ground voltage V_{agnd}), signaling the end of the time period t_2. A counter, operated on ϕ_{clk}, digitizes the time intervals and sets the nominal ADC resolution. The value of I_{WE} can then be calculated from $(t_2/t_1)I_{ref}$. Auto-zeroing, in which the integrator offset is sampled prior to digitizing the cell current, can be performed by setting the ϕ_{az} signal appropriately. This procedure implements offset correction, mitigating the effect of $1/f$ noise on the output, and helps to reduce mismatch among sensor sites, leading to a decrease in "fixed-pattern" noise.

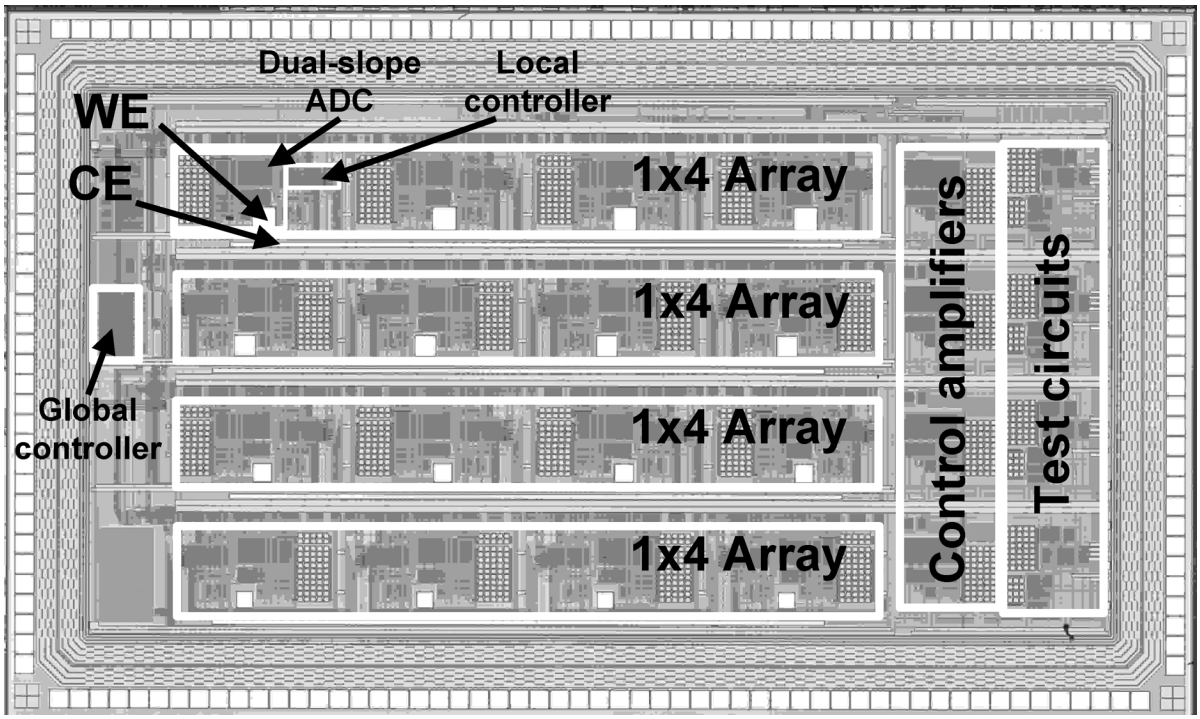

Fig. 5. Die photograph of the active CMOS sensor array.

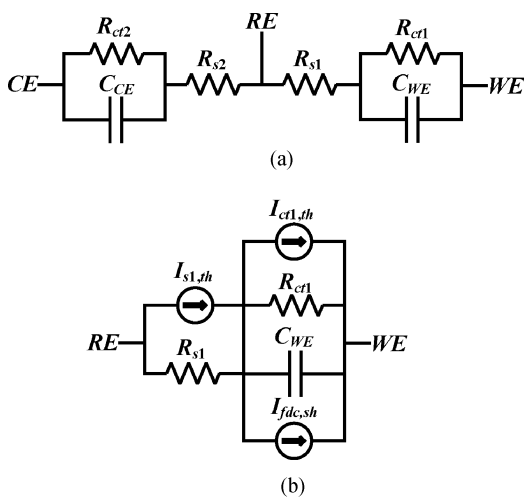

Fig. 6. Small-signal circuit models of (a) the electrode–electrolyte interfaces present in an electrochemical cell and (b) the WE–electrolyte interface augmented with noise sources.

The integrator opamp has the same architecture as the control amplifier, with identical input transistor sizes to reduce $1/f$ noise. To maintain closed-loop stability, this opamp is compensated with a 25 pF metal–insulator–metal (MIM) capacitor C_c in series with a 150-Ω polysilicon resistor R_c between the first and second stages. Based on simulations of the electrochemical interface circuit model, in which the component values are varied around their experimentally measured values, an absolute minimum simulated phase margin of 45° is obtained. This procedure also takes into account component process, voltage, and temperature (PVT) variation as well as the effect of the input impedances of all other WEs and ADCs in the array during parallel operation. In addition, extensive transient simulations are carried out to ensure stability when large-signal inputs are applied to the electrochemical cell, as required in CV.

The total bias current required by the integrator opamp is a relatively large 4 mA. Despite this, a temperature increase of only 3.5 °C is observed when the chip is performing electrochemical measurements with all ADCs running simultaneously. In addition, no deleterious effects have been witnessed during biomolecular-detection experiments due to this temperature increase.

The track-and-latch comparator following the integrator is verified in simulation to make correct decisions with a ϕ_{clk} up to at least 50 MHz. Transistors M_3 and M_4 separate the cross-coupled switching transistors at the output from the drains of input transistors M_1 and M_2 to reduce kickback interference. The latter transistors have a width and length of 200 μm and 1 μm, respectively, to reduce offset due to mismatch.

Integrated transconductance amplifiers have been included to test the operation of the ADCs. Each amplifier contains an opamp driving the gate of a large nMOS or pMOS transistor (depending on the desired current direction) with its inverting input connected to an off-chip 10-MΩ resistor that is connected to either the supply voltage or ground. The feedback loop ensures that the applied voltage at the non-inverting input is established across the resistor. Currents up to 150 nA can then be forced into the ADC using full-rail input voltages.

C. Chip Post-Processing, Packaging, and Experimental Setup

Post-processing of the fabricated chip is necessary to create an array of Au electrodes on the surface. Au has the advantage of being relatively electrochemically inactive in the presence of strong electrolytes and is easily modified by self-assembly

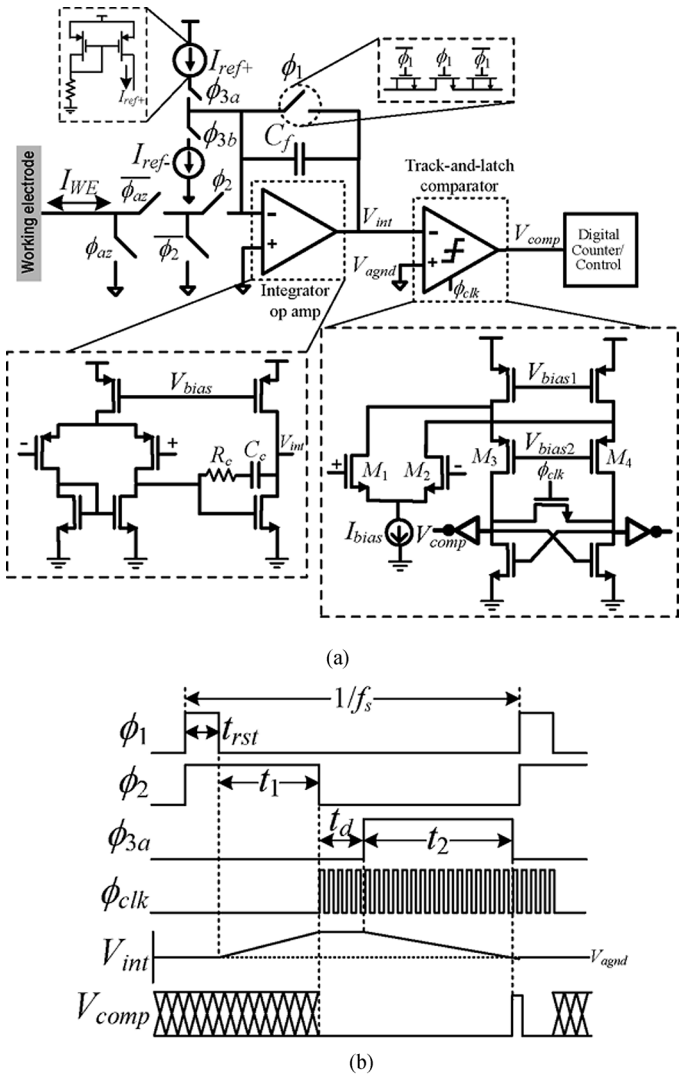

Fig. 7. Dual-slope ADC connected to each WE in the array. (a) ADC architecture. (b) ADC control signals and outputs during a typical conversion cycle (not to scale).

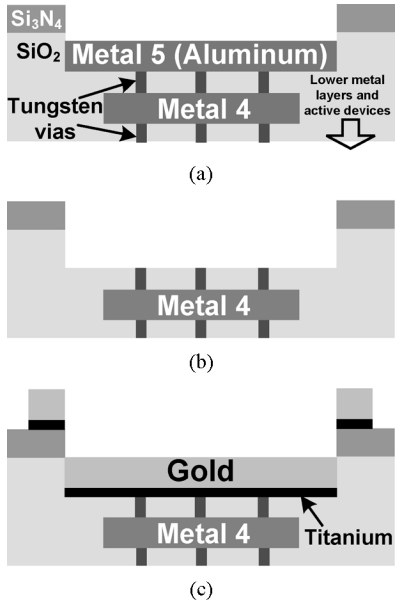

Fig. 8. CMOS post-processing steps used in fabricating the surface electrode array. (a) Cross section of the CMOS die before post-processing showing top two Al metal layers at one electrode site. (b) Result of wet etch to remove top Al metal layer. (c) Final electrode resulting from Ti–Au thin-film deposition.

of well-ordered monolayers of thiol, sulfide, or disulfide compounds through Au-sulfur bonding [8]. As a result, thiolated ssDNA probes can be bound strongly to Au surfaces.

At the time of layout, openings in the chip passivation layers are defined at the desired electrode sites above the top-metal aluminum (Al) layer in a manner similar to that used for making bond pads or probe pads, as shown in Fig. 8(a). Al is an electrochemically-active metal that is easily corroded and must be replaced as the electrode metal. After chip fabrication, the WEs are post-processed in a cleanroom environment by first selectively removing the exposed Al metal at the electrode sites using a wet-etch process as displayed in Fig. 8(b). This is followed by the electron-beam deposition of 20 nm of titanium (Ti) (which acts as an adhesion layer) and 300 nm of Au, followed by a lift-off process to form the final electrodes in Fig. 8(c). These connect directly to the tungsten (W) vias of the CMOS back end. Our method of electrode fabrication requires fewer lithographic steps than the construction of a "stepped" electrode structure [22], [23] and does not require the implementation of a full CMOS back-end process [24]. The CEs are fabricated in a similar way as the WEs.

The post-processed chip is set in a BGA package with the die surface exposed. The bond wires are shielded from electrolyte exposure through encapsulation in a heat-cured, chemical-resistant epoxy. The packaged chip is fastened in a surface-mount PCB socket with a top-plate. A 1-mm-thick polydimethylsiloxane (PDMS) sheet is introduced between the chip and top-plate to prevent electrolyte leakage onto the PCB. A glass tube is attached to the top-plate using epoxy to form an electrolyte reservoir above the chip.

IV. Experimental Results

This section contains measured results from electrical characterization of the active CMOS sensor array, along with results from electrochemical experiments involving redox species and DNA detection.

A. Potentiostat Electrical Characterization

Fig. 9 shows the output noise spectrum of the control amplifier over a bandwidth from 10 Hz to 21 kHz when this device is operated in a unity-gain configuration. The corner frequency is located around 10 kHz. The measured output noise voltage is 21.2 μV_{rms} over the 10 Hz to 21 kHz band when the effect of 60 Hz line interference and other interfering tones are neglected.

Characterization of the dual-slope ADC at each sensor site is carried out using the on-chip test circuits. To allow sufficient bandwidth for CV experiments, the ADCs are operated at an f_s of 2.5 kHz with ϕ_{clk} set to 3.5 MHz. Integration time t_1 is set to 23 μs and discharge time t_2 is allowed a maximum value of 315 μs, providing a nominal resolution of 10 bits. Although dual-slope ADCs generally feature resolutions of 16 bits or more, they are operated at very low sampling rates (a few Hz)

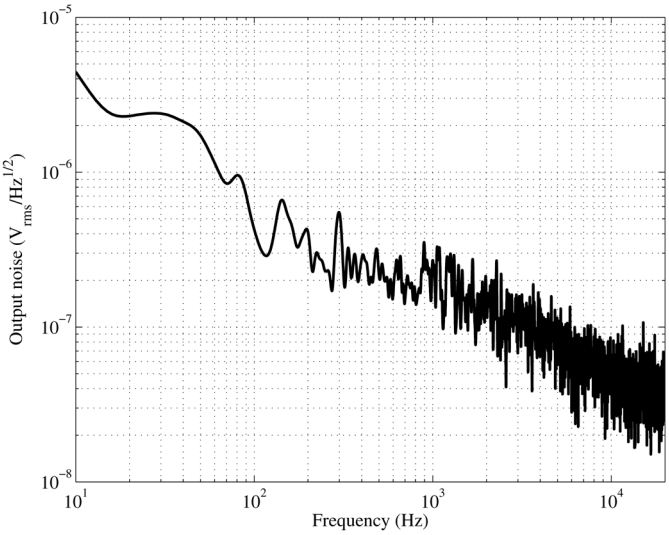

Fig. 9. Output noise spectrum of the control amplifier from 10 Hz to 21 kHz with interference tones removed.

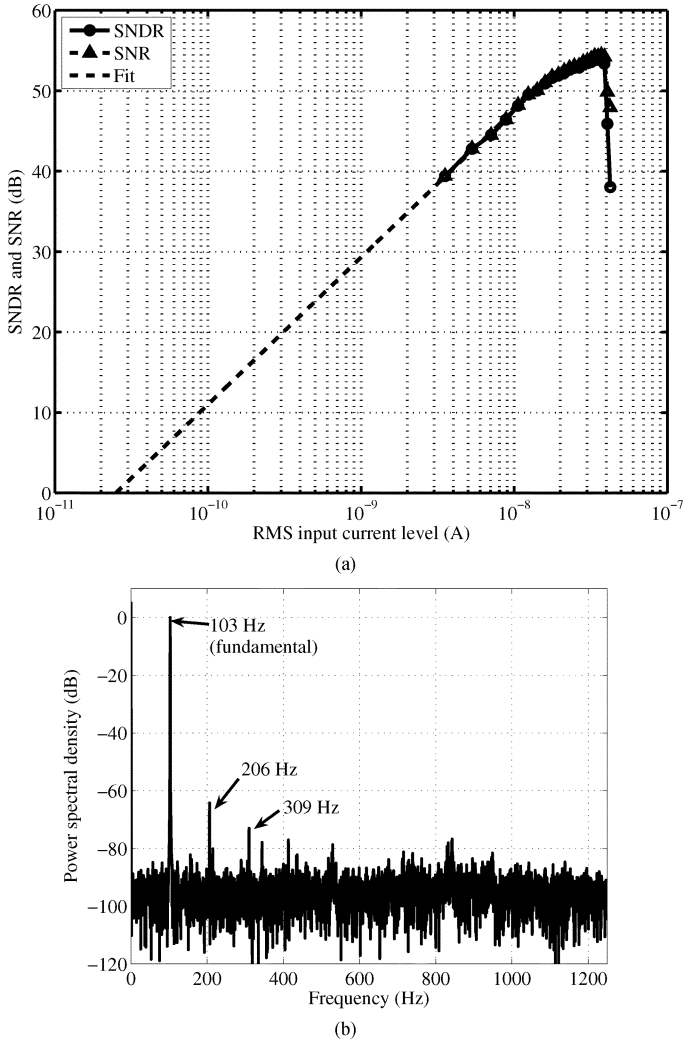

Fig. 10. Typical experimentally-measured results from ac linearity testing of the dual-slope ADC. (a) Dynamic range. (b) Output spectrum with a full-scale input at 103 Hz (resolution bandwidth is 0.31 Hz).

to avoid use of an impractically high ϕ_{clk}. Because we want to reduce the amount of on-chip switching interference due to a fast ϕ_{clk} and use a relatively high sampling rate, we have traded off resolution to achieve these goals. The remaining time during each conversion cycle is required to reset C_f and select the appropriate reference current source. The maximum I_{WE} before integrator saturation using these settings is about 110 nA. Reference currents I_{ref+} and I_{ref-} are set to 15 nA and 18 nA, respectively. Typical DNL and INL values for the ADCs are -0.25 LSB and $+0.38$ LSB, respectively, with an LSB current of approximately 240 pA.

Dynamic range (DR) of the ADC is experimentally verified using a 103 Hz sinusoidal input current. Fig. 10(a) displays the typical SNR and SNDR of the ADC as a function of input current level. The lower end of the DR curve is fitted due to the inability to provide a sufficiently small ac voltage signal to the on-chip transconductance amplifiers for ADC testing. The DR is limited at the high end by integrator saturation. A maximum effective resolution (ENOB) of 9 bits is achieved and is limited by the linearity of the test circuits. A DR of greater than 10 bits is achieved from circuit simulations of the dual-slope ADC alone. Fig. 10(b) shows the result of an 8192-point FFT of the measured ADC output when a full-scale input is applied. The strong second harmonic is due to the single-ended architecture of the ADC.

B. Cyclic Voltammetry of Potassium Ferricyanide

The redox species potassium ferricyanide, $K_3[Fe(CN)_6]$, is often used by electrochemists to study interfacial properties due to its highly reversible behavior. At the appropriate potential, ferricyanide ions are reduced to ferrocyanide ions in the reaction $Fe(CN)_6^{3-} + e \rightarrow Fe(CN)_6^{4-}$. As a first example of the use of the active CMOS sensor array for electrochemical sensing, CV measurements of 2 mM potassium ferricyanide in 1-M PPB (pH 7.4) are carried out. In these experiments, the potential between all the WEs in the array (held at 1.25 V relative to a 0 V ground) and the RE is scanned from $+0.75$ V to -0.5 V and back at various rates while the cell current is observed at one WE. To extend the potential range of the electrochemical cell beyond the 2.5 V supply limit, an off-chip, discrete control amplifier driving a Pt-wire CE and an Ag/AgCl/3-M NaCl RE is used. Prior to running the electrochemical experiments, the chip is placed in an ultraviolet/ozone cleaner for 5 min and then rinsed thoroughly in deionized water to remove organic contaminants from the surface [25].

Fig. 11(a) shows the cell current at one of the 100 μm WEs when an input scan rate ν of 72 mV/s is used. A zero-phase, low-pass FIR filter is used to post-process the raw data in MATLAB. The location of the forward (reduction) and reverse (oxidation) current peaks at $+0.22$ V and $+0.30$ V, respectively, match those obtained when the same experiment is run on a commercial potentiostat using a 125-μm-diameter Au WE. In addition, the 80 mV difference in peak potentials is relatively close to the theoretical value of 59 mV for a fully reversible, single-electron redox process [20]. The magnitude of the current falls after

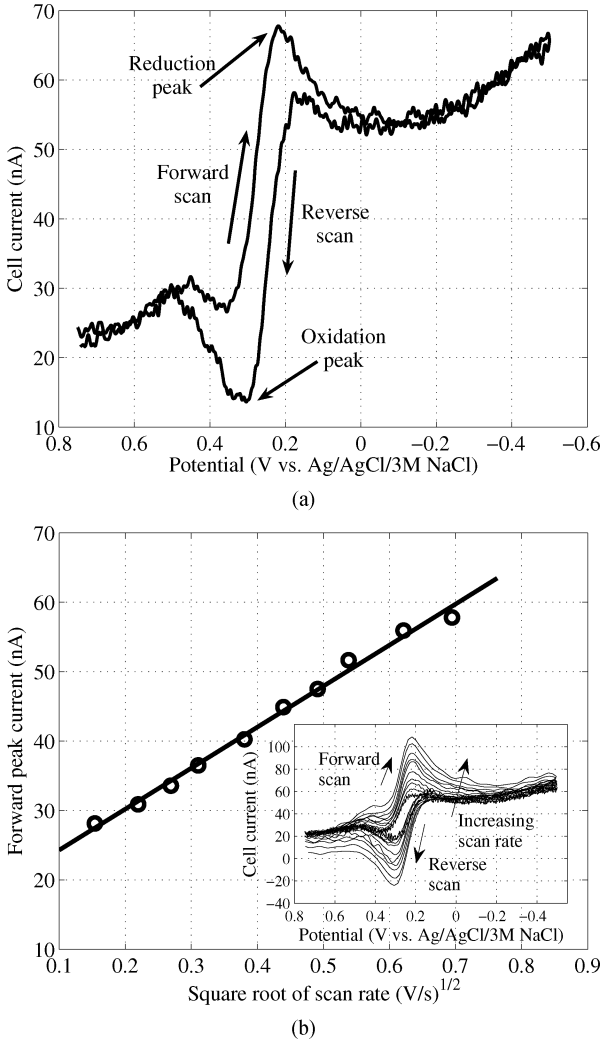

Fig. 11. CV measurements of potassium ferricyanide solution using the CMOS sensor array. (a) Measured result at a 100 μm WE at a scan rate of 72 mV/s. (b) Peak current dependence of ferrocyanide reduction on scan rate.

each peak due to mass-transport limitations of the redox species to the WE surface.

In Fig. 11(b), ν is increased from 24 mV/s to 480 mV/s and the peak reduction current is measured. It has been shown that the peak current i_p at a planar electrode for a reversible reaction under diffusive control exhibits the relationship $i_p \propto AD_O^{1/2}C_O^*\nu^{1/2}$, where A is the WE area, and D_O and C_O^* are the diffusion coefficient and bulk concentration of the oxidized species, respectively [20]. Therefore, i_p (measured after subtracting the charging current background) increases linearly with $\nu^{1/2}$, as is observed in Fig. 11(b).

The linear dependence of i_p on WE area is also verified by running a CV scan at 290 mV/s and observing the current flowing through the 100, 90, and 80 μm WEs. Fig. 12 shows the results from this measurement. Surface roughness of the electron-beam-deposited Au layer causes the actual electrode area to be larger than its geometric (drawn) area by a factor of about 1.5. This has been accounted for in the measured results.

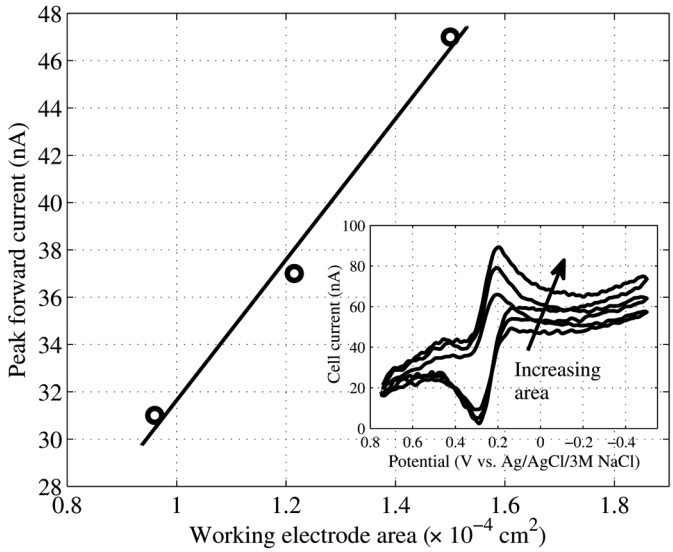

Fig. 12. Dependence of peak current from ferricyanide reduction on the WE area.

C. Determination of DNA Probe Surface Density

To demonstrate the use of the active CMOS array for biomolecular detection, the Au WEs are functionalized with a monolayer of ssDNA probes. CV measurements are then carried out in the presence of the redox species hexaammineruthenium(III) chloride (RuHex^{3+}) to determine probe surface density. The redox-active counterion RuHex^{3+} associates with the surface-immobilized DNA, causing the thermodynamics of the redox processes to be altered as a result. Prior work has shown that as probe coverage increases, the reduction potential for the reaction $\mathrm{RuHex}^{3+} + e \rightarrow \mathrm{RuHex}^{2+}$ shifts toward more negative values due to ionic spatial distributions [26]. Once calibrated, these measurements can be used to determine the probe surface coverage.

The chip is cleaned as described previously and is then incubated for 30 min in a 1-M MgCl_2 solution containing a known concentration of thiolated, 20-mer, poly-TC DNA probe. Next, the chip is incubated in 1 mM mercaptopropanol (MCP) solution for 90 min, forming a self-assembled monolayer which helps to passivate the WE surface and prevent nonspecific interactions between the immobilized DNA and WE [27]. CV at a ν of 4 V/s is then carried out in 7 mL of 10 mM Tris buffer (pH 7.4) with 1 $\mu\mathrm{M}$ RuHex^{3+}.

Fig. 13 shows the results from two different CV experiments at one 90-μm WE for DNA probe coverages of 1×10^{13} cm^{-2} and 4×10^{12} cm^{-2}. These probe densities are obtained by incubating the chip in different concentrations of DNA probe solution and are verified using a set of calibration measurements on a commercial potentiostat with 125-μm-diameter Au WE. The overall shape of the CV curves is different than those obtained in the previous section because, in this case, RuHex^{3+} is a surface-adsorbed species which is not subject to mass-transport limitations [20].

The forward peaks occur at -277.2 mV and -294.8 mV for the lower and higher probe coverages, respectively. This indicates a shift of 17.6 mV toward more negative potentials with

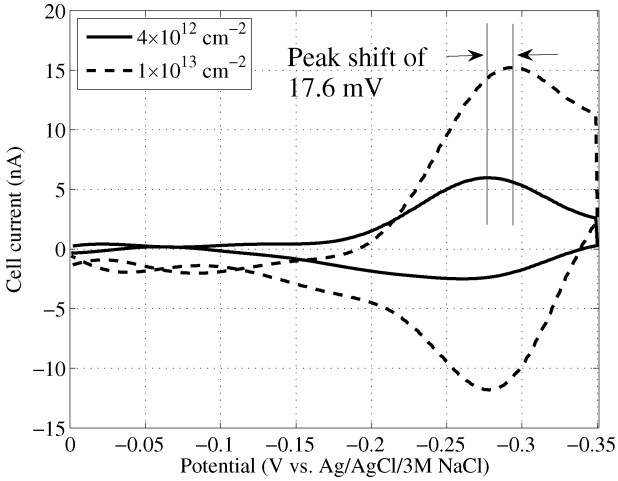

Fig. 13. DNA probe surface density measurements using RuHex^{3+}.

the higher coverage, confirming previous observations. Parallel experiments on a commercial potentiostat show similar peak potentials and a closely-matching shift of 15.4 mV. In addition, the quantity of RuHex^{3+} near the WE increases with higher probe coverages [26], as is evident in the observed peak-current increase for the 1×10^{13} cm^{-2} curve.

D. Detection of DNA Probe-Target Hybridization

Quantitative detection of DNA probe-target hybridization is carried out using the active CMOS sensor array. Single-stranded, 18-mer DNA target molecules are each conjugated with a single ferrocene (Fc) redox label that undergoes the reaction Fc $\leftrightarrow$ Fc$^+ + e$ over a well-defined potential range [28]. When labeled targets are introduced into a system containing surface-bound probes, the number of target molecules that hybridize is determined by an equilibrium that depends on such factors as the relative probe and target concentrations, buffer ionic strength, and temperature [29], [30]. After hybridization, the amount of bound target is measured from the charge transferred due to the Fc reaction, with one electron contributed by each probe-target pair on the WE surface. This value can be determined from CV measurements by integrating the area enclosed by the Fc redox current after subtraction of background charging contributions, and then dividing the result (in Coulombs) by the magnitude of the electronic charge. This method differs from "intercalation"-based approaches to DNA detection [17] which do not provide a measure of the amount of probe-target hybridization on the WE surface.

For the following DNA hybridization detection experiments, the cell potential is scanned from zero to $+0.35$ V and back at a ν of 60 V/s. Due to the relatively high scan rate required, f_s of the dual-slope ADCs is increased to 10 kHz with ϕ_{clk} set to 3.5 MHz. The fixed integration and maximum discharge times are 15 μs and 63 μs, respectively, with both reference current sources set to approximately 60 nA. At this setting, the typical measured SNDR is 43.7 dB at a current a level of 38 nA_{rms} (corresponding to a level of -6 dBFS) and the maximum DNL and INL are $+0.22$ LSB and $+0.15$ LSB, respectively.

The chip is cleaned, then incubated in a 0.50-μM solution of 20-mer ssDNA probe that codes for a section of the gene that causes retinoblastoma (RB1), a form of eye cancer in humans,

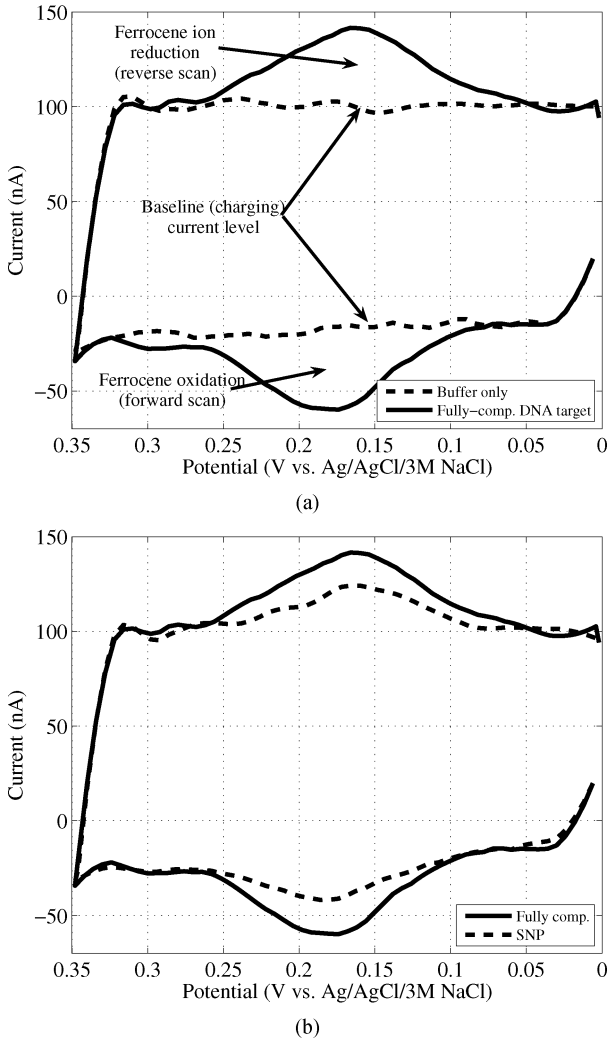

Fig. 14. Detection of DNA probe-target hybridization using the CMOS sensor array. (a) CV results showing baseline current and signal current after Fc-labeled targets have hybridized with probes at one 100 μm WE in the array. (b) Comparison of CV results with fully complementary target and target containing a SNP.

and is then incubated in MCP. The sensor array is operated in 1-M PPB and the baseline current level at a 100 μm WE is first measured as shown in Fig. 14(a). Hysteresis causes the forward and reverse charging currents to differ. Based on the average charging current level, the WE interfacial capacitance is approximately 7 μF cm^{-2}, which is in the expected range for a surface-modified Au electrode [26].

A solution of Fc-labeled target DNA, having a sequence of DNA bases that is fully complementary to that of the probe, is added to the electrolyte so that the overall target concentration is 6 nM. After 60 min the signal stabilizes and current peaks are evident from the Fc-labeled targets that have bound to the probes, as shown in Fig. 14(a). Based on the area enclosed by the redox signal and baseline current, the surface density (coverage) of hybridized targets is 3.03×10^{12} cm^{-2}.

In a second experiment, the same procedure as above is followed; however, a DNA-target sequence having a single-base mismatch compared to the probe is used. Sensor specificity in the presence of these single-nucleotide polymorphisms (SNPs) is important for genetic testing, in which mutations are

characterized by single (or few) base-pair changes. Fig. 14(b) displays the resulting CV curve using the single-mismatch target sequence along with the curve obtained from the fully complementary target for comparison. Because the target containing the SNP has less affinity for the probe, a smaller fraction of target is hybridized, as can be seen from the reduced signal level in Fig. 14(b). The target coverage in this case is 1.59×10^{12} cm^{-2}.

Sensor detection limit and noise analysis. The minimum target coverage that can be measured by the CMOS sensor array is limited by electrochemical noise processes [31], noise from the integrated electronics, ADC quantization noise, and uncertainties arising from cross-hybridization due to nonspecific binding during operation in a multi-target analyte [32]. Since this last noise source is too complex to consider here, we will focus on how the remaining three affect the sensor detection limit.

It can be shown that the maximum current $I_{\max}$ produced during CV of an electroactive, surface-bound species, like Fc-labeled DNA targets, may be expressed using [20]

$$I_{\max} = \frac{n^2F^2}{4RT}\nu A\left(\frac{D}{N_A}\right) \tag{1}$$

where n is the number of electrons transferred by the electroactive species (one for the Fc reaction), F is the Faraday constant, R is the molar gas constant, T is the absolute temperature, A is the WE area, D is the target coverage density, and N_A is Avogadro's number.

The quantization-noise-free detection limit of the active CMOS sensor array can be determined by finding the D which produces a signal-to-noise ratio (SNR) of three [33] at the output of the integrator opamp in Fig. 7(a). The SNR of the sensor is given by

$$\mathrm{SNR} = \frac{\overline{V_{o,\max}^2}}{\overline{V_{o,th}^2} + \overline{V_{o,sh}^2} + \overline{V_{dis}^2} + \overline{V_{rst}^2} + \overline{V_{amp}^2}}. \tag{2}$$

The variables in the above expression are as follows. $\overline{V_{o,\max}^2}$ is the mean square voltage at the integrator output when the signal current $I_{\max}$ is produced. $\overline{V_{o,th}^2}$ is the mean square voltage at the integrator output due to thermal noise currents produced by resistors in the electrochemical cell noise model in Fig. 6(b) [14]. Only noise sources associated with the WE–electrolyte interface are included because of the virtual ground provided by the potentiostat control loop at the RE. $\overline{V_{o,sh}^2}$ is the mean square voltage at the integrator output due to shot noise when $I_{\max}$ flows. Shot noise is known to occur during Faradaic processes [31] and can be modeled as a current source $I_{fdc,sh}$ having a two-sided power spectral density (PSD) of qI_{fdc}, where I_{fdc} is the cell Faradaic current, as shown in Fig. 6(b). $\overline{V_{rst}^2}$ arises from kT/C_f noise when the integration capacitor is reset. $\overline{V_{dis}^2}$ represents the thermal noise produced by the appropriate current mirror transistor [operating in saturation and having a two-sided PSD of $2kT(2/3)g_m$, where g_m is the transistor transconductance] used to discharge C_f during the period t_2 of the dual-slope conversion cycle. Finally, $\overline{V_{amp}^2}$ is the input-referred thermal noise of the integrator opamp. To simplify the analysis, we have assumed all the above noise sources are uncorrelated and that the small-signal parameters of the electrochemical cell remain fixed over the input voltage range. In addition, we have neglected charging currents (which are removed when calculating D), the relatively insignificant switch on-resistance noise contributions, opamp $1/f$ noise (because we have optimized for this), and comparator input-referred noise. We also further simplify the analysis by considering only $I_{\max}$, which eliminates the benefits from averaging when the overall redox current response (like that shown in Fig. 14) is integrated to obtain the total charge transferred.

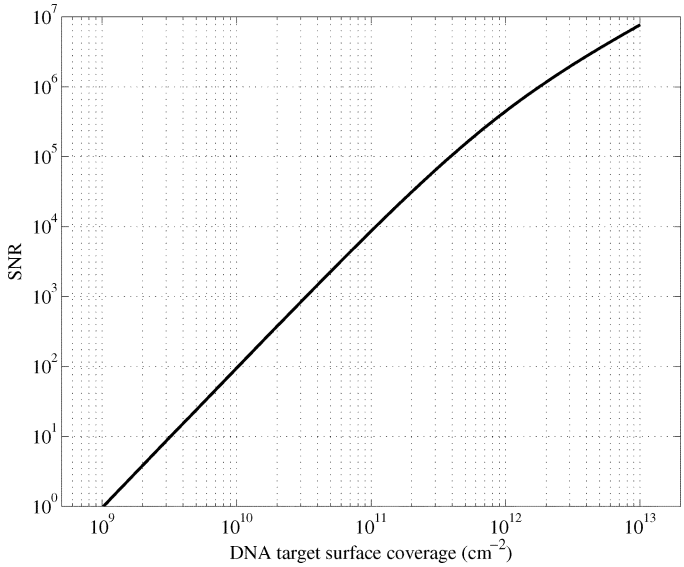

Fig. 15. Computed quantization-noise-free SNR of active CMOS sensor as a function of DNA target coverage.

The mean square voltage signal $\overline{V_{o,\max}^2}$ is given by $\overline{I_{\max}^2}(t_1/C_f)^2$, where $\overline{I_{\max}^2}$ is the mean square maximum redox current. Because the integrator output voltage is not in steady state, $\overline{V_{o,th}^2}$ at the end of the integration period t_1 is given by

$$\overline{V_{o,th}^2(t_1)} = \frac{P_{I_{th}}}{2}\frac{t_1}{C_f^2} \tag{3}$$

where $P_{I_{th}}/2$ is the two-sided PSD of the total thermal noise current produced by the electrochemical cell, and is given by (5) in the Appendix. The shot noise term $\overline{V_{o,sh}^2}$ can be computed similarly and is expressed using

$$\overline{V_{o,sh}^2(t_1)} = \frac{P_{I_{sh}}}{2}\frac{t_1}{C_f^2} \tag{4}$$

in which $P_{I_{sh}}/2$ is the two-sided PSD of the shot noise current flowing through the WE and is given by (6) in the Appendix. The mean square noise $\overline{V_{dis}^2}$ with two-sided PSD $P_{I_{dis}}/2$ is found as in (3) and (4), except that t_2 is substituted for t_1. The derivation of (3) and (4) is included in the Appendix.

Fig. 15 shows the resulting sensor SNR evaluated as a function of D. Assuming a 100 μm WE, the same CV experimental conditions and ADC settings described previously in this section, that $R_{s1} = 275\ \Omega$ and $R_{ct1} = 10\ \mathrm{M}\Omega$ (based on measured values in Section III), and that $T = 298$ K, we have computed $\overline{V_{rst}} = 28.7\ \mu\mathrm{V}_{rms}$ and $\overline{V_{o,th}} = 22.2\ \mu\mathrm{V}_{rms}$, which are independent of D. In addition, $\overline{V_{amp}}$ stays relatively constant

as a function of D, equalling approximately 23.0 μV_{rms}. We have also found that $\overline{V_{o,sh}}$ and $\overline{V_{dis}}$ exceed the rms sum of $\overline{V_{rst}}$, $\overline{V_{o,th}}$, and $\overline{V_{amp}}$ starting at coverages of about 1.4×10^{12} cm^{-2} and 2.4×10^{12} cm^{-2}, respectively, based on this analysis. This can be observed in the "compression" of the SNR curve in Fig. 15 which begins to occur at coverages in the 10^{12} cm^{-2} range. An SNR of three is obtained when D is approximately 1.8×10^{9} cm^{-2}, or 18 μm^{-2}. The corresponding $I_{\max}$ at this SNR is about 25 pA$_{rms}$.

Based on DR measurements of the dual-slope ADC with the present settings, the smallest current level that can be detected with an SNR of three is approximately 550 pA$_{rms}$. Therefore, the estimated detection limit of our active CMOS sensor array (implemented using a 10-bit ADC) is about 22 times higher than the quantization-noise-free limit, and equals approximately 4×10^{10} cm^{-2}, or 400 μm^{-2}. As a result, a Nyquist-rate-ADC resolution of almost 15 bits would be required to operate the sensor in a thermal- and shot-noise-limited regime. Although implementation of very-high-resolution converters may help bridge the gap between the present detection limit and that provided by fluorescence-based sensing techniques (which feature detection limits down to 0.1 μm^{-2}), this presents a significant engineering challenge. Therefore, the use of alternative chemical protocols for label-based detection (such as attaching multiple redox labels to each target strand [34]) may be a more feasible solution.

V. Conclusion

Active CMOS electrochemical sensor arrays for biomolecular detection eliminate the need for the bulky and expensive optical equipment used in fluorescence-based microarrays. Such a reduction in size and complexity paves the way for the use of electrochemical sensor arrays in point-of-care applications. This paper presented the design of a four-by-four array implemented in a standard 0.25-μm CMOS process augmented by post-processing to fabricate integrated electrochemically compatible electrodes. Integrated potentiostat electronics and ADCs stimulate and measure electrochemical reactions occurring at the chip surface. Experimental results from CV measurements of redox species, characterization of DNA probe coverages, and quantitative and specific detection of DNA probe-target hybridization demonstrated the bio-diagnostic prospects of the chip.

Appendix

The thermal noise currents $I_{s1,th}$ and $I_{ct1,th}$ produced by the resistors R_{s1} and R_{ct1}, respectively, in Fig. 6(b), can each be modeled as a zero-mean, wide-sense stationary (WSS), white Gaussian noise process with a two-sided PSD of $2kT/R$, in which R is the appropriate resistor. The two-sided PSD of the total thermal noise $P_{I_{th}}/2$ flowing through the WE interface can then be expressed as

$$\frac{P_{I_{th}}}{2} = \frac{2kT}{R_{s1} + R_{ct1}} \tag{5}$$

assuming that all the noise processes are uncorrelated.

The shot noise produced by redox current in an electrochemical cell can be modeled like the thermal noise process above and has a two-sided PSD of $qI_{\max}$. The two-sided PSD of the shot noise flowing through the WE interface $P_{I_{sh}}/2$ is given by

$$\frac{P_{I_{sh}}}{2} = \frac{R_{ct1}^2 q I_{\max}}{(R_{s1} + R_{ct1})^2}. \tag{6}$$

For a zero-mean, WSS, white noise current process $I(t)$, the output noise voltage $V_o(t)$ from an integrator with feedback capacitor C starting at time $t = 0$ is given by [35]

$$V_o(t) = \frac{1}{C} \int_0^t I(\tau)\, \mathrm{d}\tau. \tag{7}$$

The mean square voltage $\overline{V_o^2(t)}$ can be found as follows:

$$\begin{aligned} \overline{V_o^2(t)} &= \frac{1}{C^2} \int_0^t \int_0^t \overline{I(t_1) I(t_2)}\, \mathrm{d}t_1 \mathrm{d}t_2 \\ &= \frac{1}{C^2} \int_0^t \int_0^t R_I(t_1 - t_2) \mathrm{d}t_1\, \mathrm{d}t_2 \\ &= \frac{1}{C^2} \int_{-t}^t (t - |\tau|) R_I(\tau)\, \mathrm{d}\tau, \end{aligned} \tag{8}$$

where $R_I(\tau)$ is the autocorrelation function of the noise process. If $I(t)$ has the two-sided PSD $P/2$, then $R_I(\tau) = (P/2)\delta(\tau)$, given an infinite bandwidth. As a result,

$$\begin{aligned} \overline{V_o^2(t)} &= \frac{1}{C^2} \int_{-t}^t (t - |\tau|) \frac{P}{2} \delta(\tau)\, \mathrm{d}\tau \\ &= \frac{P}{2} \frac{t}{C^2}. \end{aligned} \tag{9}$$

This results in (3) and (4), where $P/2$ is given by the expressions in (5) and (6), respectively.

References

[1] M. Schena, R. A. Heller, T. P. Theriault, K. Konrad, E. Lachenmeier, and R. W. Davis, "Microarrays: Biotechnology's discovery platform for functional genomics," *Trends Biotechnol.*, vol. 16, no. 7, pp. 301–306, Jul. 1998.

[2] J. D. Hoheisel, "Microarray technology: Beyond transcript profiling and genotype analysis," *Nature Reviews Genetics*, vol. 7, pp. 200–210, Mar. 2006.

[3] S. P. A. Fodor, R. P. Rava, X. C. Huang, A. C. Pease, C. P. Holmes, and C. L. Adams, "Multiplexed biochemical assays with biological chips," *Nature*, vol. 364, pp. 555–556, Aug. 1993.

[4] M. Schena, *Microarray Analysis*. Hoboken, NJ: Wiley, 2003.

[5] T. G. Drummond, M. G. Hill, and J. K. Barton, "Electrochemical DNA sensors," *Nature Biotechnology*, vol. 21, no. 10, pp. 1192–1199, Oct. 2003.

[6] J. Wang, "Electrochemical nucleic acid biosensors," *Analytica Chimica Acta*, vol. 469, pp. 63–71, 2002.

[7] D. A. Di Giusto, W. A. Wlassoff, S. Giesebrecht, J. J. Gooding, and G. C. King, "Enzymatic synthesis of redox-labeled RNA and dual-potential detection at DNA-modified electrodes," in *Angewandte Chemie Int. Ed.*, 2004, vol. 43, pp. 2809–2812.

[8] C. Berggren, P. Stålhandske, J. Brundell, and G. Johansson, "A feasibility study of a capacitive biosensor for direct detection of DNA hybridization," *Electroanalysis*, vol. 11, no. 3, pp. 156–160, Mar. 1999.

[9] R. F. B. Turner, D. J. Harrison, and H. P. Baltes, "A CMOS potentiostat for amperometric chemical sensors," *IEEE J. Solid-State Circuits*, vol. SC-22, no. 3, pp. 473–478, Jun. 1987.

[10] R. J. Reay, S. P. Kounaves, and G. T. A. Kovacs, "An integrated CMOS potentiostat for miniaturized electroanalytical instrumentation," in *IEEE ISSCC Dig. Tech. Papers*, 1994, pp. 162–163.
[11] M. Naware, A. Rege, R. Genov, M. Stanacevic, G. Cauwenberghs, and N. Thakor, "Integrated multi-electrode fluidic nitric-oxide sensor and VLSI potentiostat array," in *Proc. IEEE Int. Symp. Circuits and Systems (ISCAS)*, 2004, pp. 25–28.
[12] W. Sansen, D. De Wachter, L. Callewaert, M. Lambrechts, and A. Claes, "A smart sensor for the voltammetric measurement of oxygen or glucose concentrations," *Sensors Actuators B*, vol. 1, pp. 298–302, 1990.
[13] M. Schienle, C. Paulus, A. Frey, F. Hofmann, B. Holzapfl, P. Schindler-Bauer, and R. Thewes, "A fully electronic DNA sensor with 128 positions and in-pixel A/D conversion," *IEEE J. Solid-State Circuits*, vol. 39, no. 12, pp. 2438–2445, Dec. 2004.
[14] S. M. Martin, F. H. Gebara, B. J. Larivee, and R. B. Brown, "A CMOS-integrated microinstrument for trace detection of heavy metals," *IEEE J. Solid-State Circuits*, vol. 40, no. 12, pp. 2777–2786, Dec. 2005.
[15] C. Stagni, C. Guiducci, L. Benini, B. Riccò, S. Carrara, B. Samorí, C. Paulus, M. Schienle, M. Augustyniak, and R. Thewes, "CMOS DNA sensor array with integrated A/D conversion based on label-free capacitance measurement," *IEEE J. Solid-State Circuits*, vol. 41, no. 12, pp. 2956–2964, Dec. 2006.
[16] M. Augustyniak, C. Paulus, R. Brederlow, N. Persike, G. Hartwich, D. Schmitt-Landsiedel, and R. Thewes, "A 24×16 CMOS-based chronocoulometric DNA microarray," in *IEEE ISSCC Dig. Tech. Papers*, 2006, pp. 46–47.
[17] N. Gemma, S. O'uchi, H. Funaki, J. Okada, and S. Hongo, "CMOS integrated DNA chip for quantitative DNA analysis," in *IEEE ISSCC Dig. Tech. Papers*, 2006, pp. 560–561.
[18] A. Hassibi and T. H. Lee, "A programmable 0.18-μm CMOS electrochemical sensor microarray for biomolecular detection," *IEEE Sensors J.*, vol. 6, pp. 1380–1388, Dec. 2006.
[19] P. M. Levine, P. Gong, K. L. Shepard, and R. Levicky, "Active CMOS array for electrochemical sensing of biomolecules," in *Proc. IEEE Custom Integrated Circuits Conf. (CICC)*, 2007, pp. 825–828.
[20] A. J. Bard and L. R. Faulkner, *Electrochemical Methods: Fundamentals and Applications*, 2nd ed. New York, NY: Wiley, 2001.
[21] D. Johns and K. Martin, *Analog Integrated Circuit Design*. New York, NY: Wiley, 1997.
[22] S. M. Martin, T. D. Strong, and R. B. Brown, "Monolithic liquid chemical sensing systems," in *Materials Research Soc. Symp. Proc. Vol. 869: Materials, Integration and Technology for Monolithic Instruments*, Mar. 2005, pp. 109–118.
[23] A. Mason, Y. Huang, C. Yang, and J. Zhang, "Amperometric readout and electrode array chip for bioelectrochemical sensors," in *Proc. IEEE Int. Symp. Circuits and Systems (ISCAS)*, 2007, pp. 3562–3565.
[24] R. Thewes, F. Hofmann, A. Frey, B. Holzapfl, M. Schienle, C. Paulus, P. Schindler, G. Eckstein, C. Kassel, M. Stanzel, R. Hintsche, E. Nebling, J. Albers, J. Hassman, J. Schülein, W. Goemann, and W. Gumbrecht, "Sensor arrays for fully electronic DNA detection on CMOS," in *IEEE ISSCC Dig. Tech. Papers*, 2002, pp. 350–351.
[25] J. R. Vig, "UV/ozone cleaning of surfaces," *J. Vacuum Sci. Technol. A*, vol. 3, no. 3, pp. 1027–1034, May 1985.
[26] G. Shen, N. Tercero, M. A. Gaspar, B. Varughese, K. Shepard, and R. Levicky, "Charging behavior of single-stranded DNA polyelectrolyte brushes," *J. Amer. Chem. Soc.*, vol. 128, no. 26, pp. 8427–8433, Jul. 2006.
[27] T. M. Herne and M. J. Tarlov, "Characterization of DNA probes immobilized on gold surfaces," *J. Amer. Chem. Soc.*, vol. 119, no. 38, pp. 8916–8920, 1997.
[28] T. Ihara, Y. Maruo, S. Takenaka, and M. Takagi, "Ferrocene-oligonucleotide conjugates for electrochemical probing of DNA," *Nucleic Acids Res.*, vol. 24, no. 21, pp. 4273–4280, Nov. 1996.
[29] R. P. Ekins and F. W. Chu, "Multianalyte microspot immunoassay-microanalytical compact disk of the future," *Clin. Chem.*, vol. 37, no. 11, pp. 1955–1967, Nov. 1991.
[30] R. Levicky and A. Horgan, "Physicochemical perspectives on DNA microarray and biosensor technologies," *Trends Biotechnol.*, vol. 23, no. 3, pp. 143–149, Mar. 2005.
[31] U. Bertocci and F. Huet, "Noise analysis applied to electrochemical systems," *Corrosion Sci.*, vol. 51, no. 2, pp. 131–144, Feb. 1995.
[32] Y. Tu, G. Stolovitzky, and U. Klein, "Quantitative noise analysis for gene expression microarray experiments," *Proc. Nat. Acad. Sci. USA*, vol. 99, no. 22, pp. 14031–14036, 2002.
[33] D. A. Skoog, F. J. Holler, and T. A. Nieman, *Principles of Instrumental Analysis*, 5th ed. Philadelphia, PA: Saunders, 1998.
[34] J. Liu, S. Tian, L. Tiefenauer, P. E. Nielsen, and W. Knoll, "Simultaneously amplified electrochemical and surface plasmon optical detection of DNA hybridization based on ferrocene-streptavidin conjugates," *Analyt. Chem.*, vol. 77, no. 9, pp. 2756–2761, 2005.
[35] H. Tian, "Noise analysis in CMOS image sensors," Ph.D. dissertation, Stanford Univ., Palo Alto, CA, 2000.

Peter M. Levine (S'99) received the B.Eng. degree in computer engineering in 2002 and the M.Eng. degree in electrical engineering in 2004 from McGill University, Montreal, Quebec, Canada. Since 2004, he has been pursuing the Ph.D. degree in electrical engineering at Columbia University, New York, NY.

His research interests include CMOS-integrated electrochemical sensors, analog/mixed-signal integrated circuit design and test, DNA microarrays, and biosensors. He has held internship positions in the areas of hardware development and integrated circuit design with Matrox Electronic Systems, Nortel Networks, and Intel.

During the 2005 and 2006 academic years, Mr. Levine was the recipient of an Intel Foundation Ph.D. Fellowship.

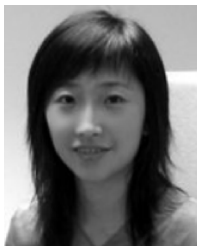

Ping Gong received the B.S. degree in chemistry from Peking University, Beijing, China, in 1999 and the Ph.D. degree in analytical chemistry from Colorado State University, Fort Collins, CO, in 2006.

She has since worked as a postdoctoral research associate at Columbia University in the Departments of Chemical and Electrical Engineering. Her research interests include the development of electrochemical methods in the characterization and quantification of surface DNA hybridization behavior for biosensing applications and the development of bio-conjugation, microarray surface fabrication, characterization, and fluorescence quantum dot detection methods for integrated CMOS biosensor applications.

Dr. Gong is a member of the American Chemical Society and the American Vacuum Society.

Rastislav Levicky received the B.S. degree in chemical engineering from Columbia University, New York, NY, in 1991, and the Ph.D. degree in chemical engineering from the University of Minnesota, Minneapolis, in 1996. His Ph.D. thesis focused on self-organized polymer brush and mesogel assemblies at solid-liquid interfaces and in thin films.

From 1996 to 1998, he was a National Research Council Postdoctoral Associate with the National Institute of Standards and Technology (NIST), Gaithersburg, MD, where he studied the interfacial organization and biological activity of polynucleic acids with neutron beam and optical techniques. In July 1998, he joined the Chemical Engineering faculty at Columbia University, and moved to the Department of Chemical and Biological Engineering at Polytechnic University, Brooklyn, NY, in July 2006. His current research interests encompass biointerfacial engineering, biomolecular diagnostics, kinetics of interfacial reaction networks, dynamic processes in polymer thin films, and electrochemistry.

Dr. Levicky is a member of the American Institute of Chemical Engineers, the American Chemical Society, the American Physical Society, the American Vacuum Society, and the Materials Research Society. He is a recipient of the Union Carbide Kenan Analytical Award, the Sigma Xi Outstanding Poster Award, the National Science Foundation CAREER Award for Young Investigators, and the 2001 Distinguished Faculty Teaching Award.

Kenneth L. Shepard (S'85–M'92–SM'03–F'07) received the B.S.E. degree from Princeton University, Princeton, NJ, in 1987, and the M.S. and Ph.D. degrees in electrical engineering from Stanford University, Stanford, CA, in 1988 and 1992, respectively.

From 1992 to 1997, he was a Research Staff Member and Manager with the VLSI Design Department, IBM T. J. Watson Research Center, Yorktown Heights, NY, where he was responsible for the design methodology for IBM's G4 S/390 microprocessors. Since 1997, he has been with Columbia University, New York, NY, where he is now a Professor. He also served as Chief Technology Officer of CadMOS Design Technology, San Jose, CA, until its acquisition by Cadence Design Systems in 2001. His current research interests include design tools for advanced CMOS technology, on-chip test and measurement circuitry, low-power design techniques for digital signal processing, low-power intrachip communications, and CMOS imaging applied to biological applications.

Dr. Shepard was the recipient of the Fannie and John Hertz Foundation Doctoral Thesis Prize in 1992. At IBM, he received Research Division Awards in 1995 and 1997. He was also the recipient of the National Science Foundation CAREER Award in 1998 and IBM University Partnership Awards from 1998 through 2002. He was also awarded the 1999 Distinguished Faculty Teaching Award from the Columbia Engineering School Alumni Association. He has been an Associate Editor of the IEEE TRANSACTIONS ON VERY LARGE SCALE INTEGRATION (VLSI) SYSTEMS and was the technical program chair and general chair for the 2002 and 2003 International Conference on Computer Design, respectively. He has served on the program committees for ICCAD, ISCAS, ISQED, GLS-VLSI, TAU, and ICCD.